TESLA FEL Report 2006-02

Finite Element Analyses for RF Photoinjector Gun Cavities

F. Marhauser

BESSY GmbH

Contents

Finite Element Analyses for RF Photoinjector Gun Cavities

F. Marhauser
BESSY, Albert-Einstein Straße 15, D-12489 Berlin, Germany

Abstract

This paper details electromagnetical, thermal and structural 3D Finite Element Analyses (FEA) for normal conducting RF photoinjector gun cavities. The simulation methods are described extensively. Achieved results are presented.

1. Introduction

RF photoinjectors are the ultimate choice to generate short electron pulses of high bunch charge with extraordinary low transverse emittance as demanded by future free electron lasers and linear colliders. As superconducting gun cavities are still a subject of research and development, normal conducting gun technology is widely used for the time being (mainly at L- or S-Band). A thermally stable operation of the gun cavity is mandatory to prevent from parasitic RF amplitude and phase jitters, which in turn are converted into energy and timing jitters of the beam bothering the performance of subsequent components of the accelerator. In these injectors the photocathode is exposed to electric fields in the range of several ten MV/m to confine space charge forces just at their origin. Operating at a high duty cycle (in the percent regime) such high field levels requires average power levels of several ten kW. Hence the cooling layout has to be severely optimized. This can be done numerically by using the multi-physics package of the FEA code ANSYS [1]. The principal FEA techniques are detailed in this paper to forecast important electromagnetic, thermal and mechanical properties of RF cavities. A comprehensive description of the calculation procedures is given in section 2. Achieved results are finally presented in section 3 for 1½-cell L-Band cavities designed at DESY, i.e. (i) *Gun 2* - successfully characterized at the Photoinjector Test Facility Zeuthen (PITZ) and currently under operation at the VUV-FEL, (ii) *Gun 4* – still under design with an improved cooling scheme aiming for an increased power level and/or duty cycle.

2. Finite Element Analyses

The multi-physics package ANSYS provides the environment for comprehensive FEA of RF cavities including electromagnetical, thermal and structural analyses. It uses a modular concept for modelling, meshing, solving and post-processing of physical problems. The technique to produce 3D solutions to RF cavity design problems in ANSYS has first been described in ref. [2]. It has been complemented by combining ANSYS and SUPERFISH [3] results to assess temperature induced frequency shifts. In this section the applied simulation procedure is described in detail taking as example *Gun 4*. Transient or non-static characteristics were not of major concern and have been disregarded.

2.1. Preparation and Import of Geometry

Compared to the computational time actually a main part of the work is dedicated to the preparation of the solid model geometries. In case a primal 3D CAD cavity model already exists (created in Pro/ENGINEER, I-DEAS, SolidWorks, Autodesk Inventor etc.) it is easily transferred to ANSYS in a capable file format. This tremendously eases the work load in contrary to the laborious ANSYS-inherent modelling effort. We have used the Pro/ENGINEER [4] to ANSYS interface for the direct import of the problem geometry. However, before transferring the 3D model to ANSYS, it has to be "purified" from dispensable parts eventually preventing from clean meshing of the solids (e.g. soldering depots, nuts and bolts, bolt holes, water inlet and outlet connectors) building up the model. This is illustrated in Figure 1 leaving just the cavity wall and intrinsic cooling meanders from the original CAD model. As far as acceptable in 3D only a portion of the cavity needs to be modelled in ANSYS making use of symmetry planes.

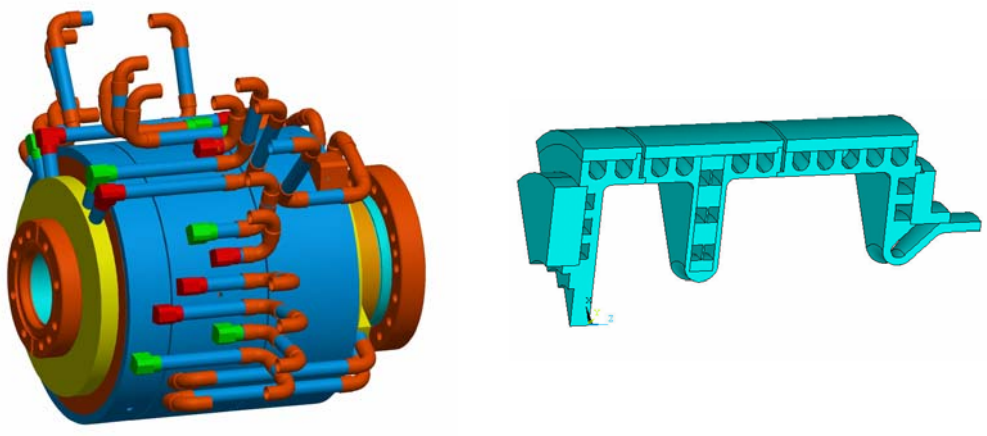

Figure 1 : Original Pro/ENGINEER cavity assembly (left) and corresponding ANSYS 1/8-model (right) just leaving the gun wall and water cooling holes. In case simplifications in 3D are acceptable, only a portion of the cavity is modeled. This not only reduces CPU time and memory usage but rather allows a finer mesh resolution to overcome prevalent meshing errors. This has to be considered especially if the maximum number of mesh nodes is limited (e.g. 128.000 only in case of the ANSYS university license).

If not already generated within the CAD program, the resonating vacuum volume has to be created from the gun wall (Figure 2) utilizing its bordering areas. In each case the resonator volume has to share its outer boundary surface with the inner boundary surface of the wall in order to pass heat flux results as a load for the subsequent thermal analysis.

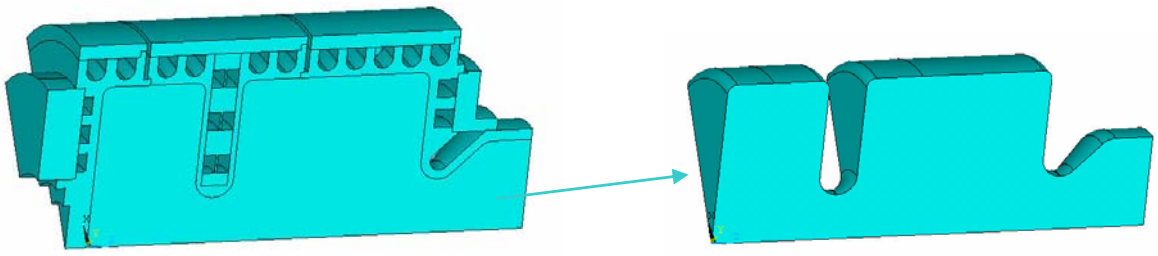

Figure 2 : The resonating volume (right) as created from the cavity wall (left) in ANSYS.

2.2. Meshing

Proper meshing of the problem geometry is mandatory for achieving reliable results. ANSYS offers different element types for meshing depending on the physics to solve. An acceptable mesh might be found by a globally defined mesh size, still having control to refine the mesh size at critical parts afterwards. Figure 3 illustrates the cavity after meshing with 3D electromagnetical tetrahedral elements in preparation of an eigenmode calculation. A global mesh size has been chosen here (Figure 3 left). A refinement of the cavity roundings has been considered (Figure 3 right) to yield a better accuracy of the electromagnetic field and heat flux results. For a more subtle mesh variation (e.g. when implementing wall openings for antennas, couplers etc.) a subdivision in various solids might be necessary [2].

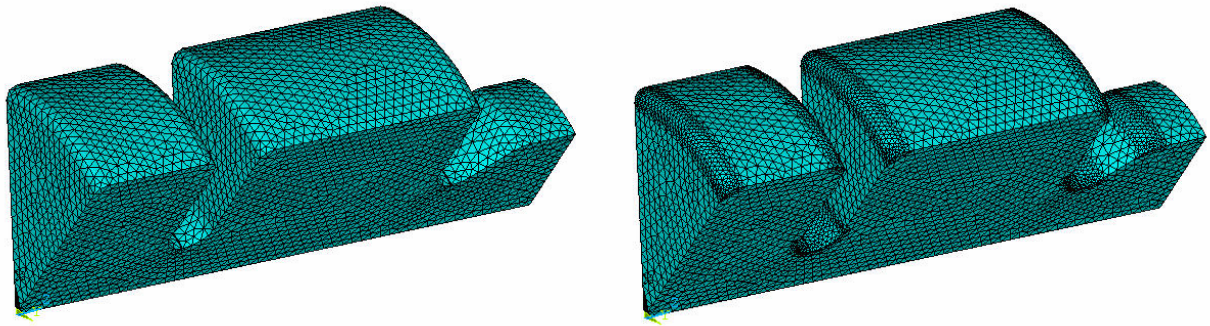

Figure 3 : Cavity meshed (3D HF119 10node electromagnetic elements) on basis of a global mesh size (left, here: 0.43 mm) and after a refinement at areas belonging to the roundings of the cavity cells, irises and beam tube (right).

2.3. Eigenmode and Heat Flux Calculation

Usually the predominant part of the thermal wall power entry of a normal conducting cavity is caused by the accelerating RF mode. The thermal load thus defines the mechanical properties of the cavity under operation. A realistic assessment of the power loss distribution along the cavity surface ("heat flux") induced by the RF magnetic field is of major importance rather than assigning surface heat fluxes 'by hand' as might be done alternatively. Thus the RF fields have been evaluated using the ANSYS inherent modal solver. Hereby Eigenmodes can be readily calculated after the material properties of the resonating volume (relative permittivity and permeability) and the electromagnetic boundary conditions have been defined. Besides an electric boundary assigned to the cavity surface, a magnetic boundary at the symmetry planes (default) is set (true for the accelerating TM_{010} π-mode of the RF gun). The Eigenwert problem is solved choosing the frequency range that encloses the mode(s) of interest. The necessary electromagnetic field solutions have to be extracted for a user-specified number of modes. Figure 4 visualizes the RF solutions of the first passband modes (0- and π-mode) of the 1½-cell cavity by means of the electric and magnetic field contours.

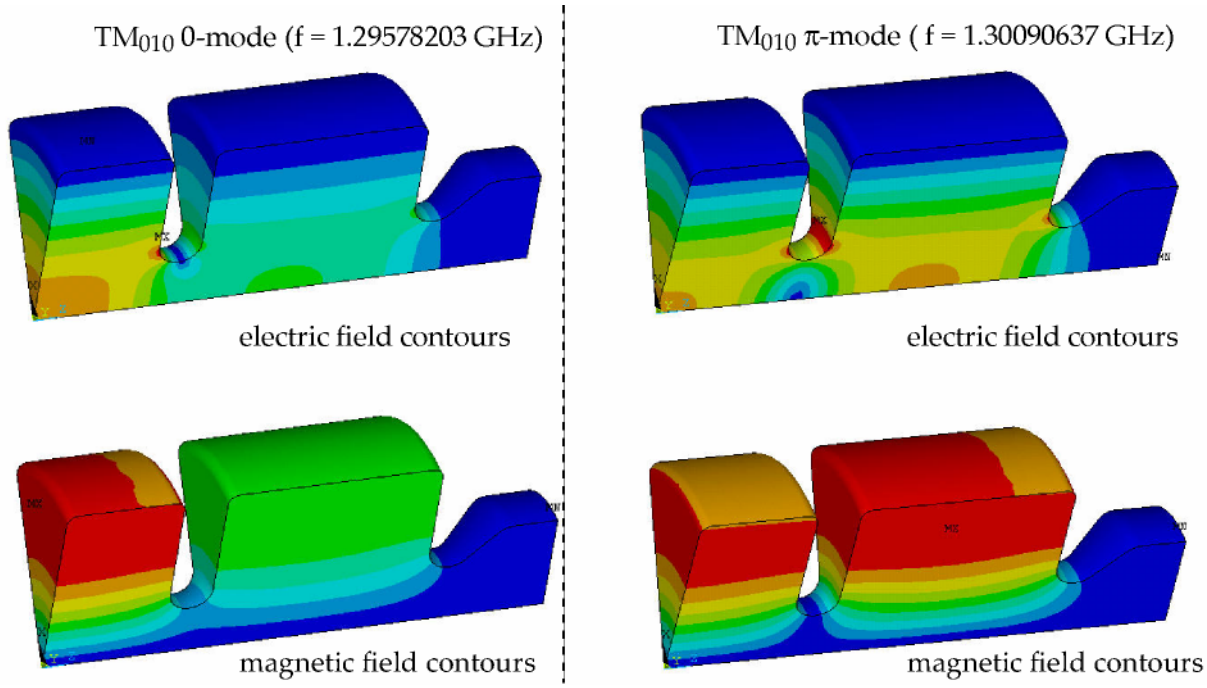

Figure 4 : Electric (top) and magnetic field contours (bottom) of the TM_{010} 0-mode (left) and π-mode (right). Absolute field levels increase from blue (minimum) to red (maximum).

In general the total ohmic wall power loss P_S can be evaluated by integrating the squared RF surface magnetic fields H along the internal cavity surface S according to

$$P_S = \frac{R_s}{2} \iint_S dS \, \vec{H}^2 , \qquad (1)$$

where R_s denotes the surface impedance to be derived from the electric conductivity σ_{el} (e.g. $\sigma_{el} = 5.8e7\ \Omega^{-1}m^{-1}$ for OFHC copper), the resonant angular frequency ω of the eigenmode and the permeability μ of the material by

$$R_S = \frac{1}{\sigma_{el}\delta_{Skin}} = \sqrt{\frac{\mu\omega}{2\sigma_{el}}} \tag{2}$$

with the skin depth

$$\delta_{Skin} = \sqrt{\frac{2}{\sigma_{el}\mu\omega}}. \tag{3}$$

By assigning R_s to the cavity shell prior to the modal analysis, the quality factor Q_0 of a given cavity mode can be calculated with an ANSYS internal macro. However, to assess the desired power loss distribution it is necessary to additionally mesh the cavity boundary surface with surface effect elements (3D thermal SURF152) exactly resembling the electromagnetical elements (see Figure 5 left). Moreover, a post processing macro had to be used (developed at BNL [2]) to calculate the heat flux for each single surface element (in W/m²) normalized by the total power value given in ANSYS according to eq. (1) and finally scaled to a user defined mean power level P_S (allowing for multiples in case only a portion of the cavity was modelled). Figure 5 right shows the principal power loss distribution in the RF gun exhibiting the strongest values at the side plates of the cavity wall. At $P_S = 100$ kW the maximum heat flux is 71 W/cm² located at the middle iris. Subsequent ANSYS calculations at different power levels can be accomplished by simply scaling the heat fluxes (defined as surface loads) without a restart of the Eigenmode solver or macro.

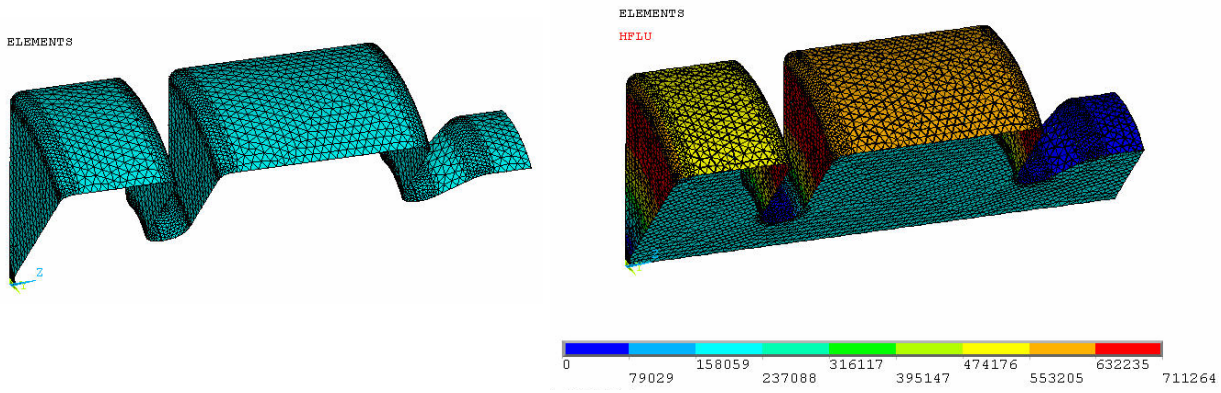

Figure 5 : 3D surface effect elements (left, i.e. SURF152) meshed upon the underlying tetrahedral mesh (HF119). The heat flux distribution is shown on the right (in W/m²) for P_S = 100 kW as calculated with a post-processing macro.

As the heat flux values represent a major input for the subsequent thermal analyses, RF solutions should possess sufficient accuracy. The data can be cross-checked by user-favoured codes with dedicated eigenmode solvers. Figure 6 and Table 1 demonstrate the excellent agreement of ANSYS RF field results with those achieved by SUPERFISH (2D) and Microwave Studio (MWS) (3D) [5] implying a properly generated mesh.

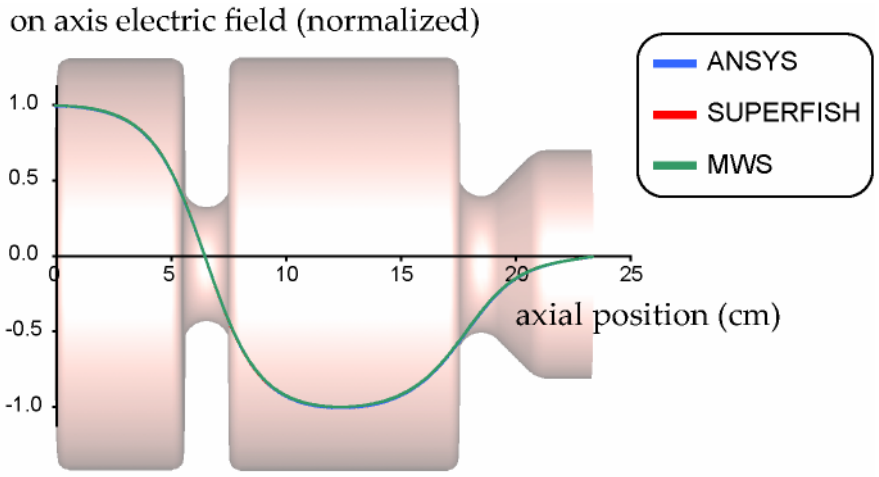

Figure 6 : Normalized on axis electric fields of the TM_{010} π-mode in the *DESY GUN 4* calculated with ANSYS (3D), MWS (3D) and SUPERFISH (2D). Data in this plot actually overlap, so that minor differences between the codes are not visible. ANSYS provides the mapping of RF field components on pre-defined paths -such as the beam axis- for graphical display or alternatively in an ASCII-formatted file.

Table 1 : Comparison of electromagnetical field results for *Gun 4* using ANSYS, MWS and SUPERFISH respectively.

Code		ANSYS 3D 1/8-model	SUPERFISH 2D	MWS 3D 1/4 -model
Number of mesh nodes/points		109022	274131	1504656
and mesh type		tetrahedral	triangular	PBA
Frequency TM_{010} π-mode	GHz	1.300906	1.300905	1.300871
Quality factor (σ = 5.8e7 $\Omega^{-1}m^{-1}$)		23486	23478	23581
Max. heat flux (R_S = 100 kW)	W/cm^2	71.127	70.725	-

2.4. Thermal Analyses

Thermal analyses requires a heat drain (here: cooling water) and a heat generation source (here: heat fluxes) to evaluate the desired temperature distribution in the problem geometry. In a first step the cavity body has to be meshed by thermal mass elements (here: tetrahedral 10node SOLID 87). The mesh "grows" upon the underlying surface effect elements which carry the heat flux information as illustrated in Figure 7.

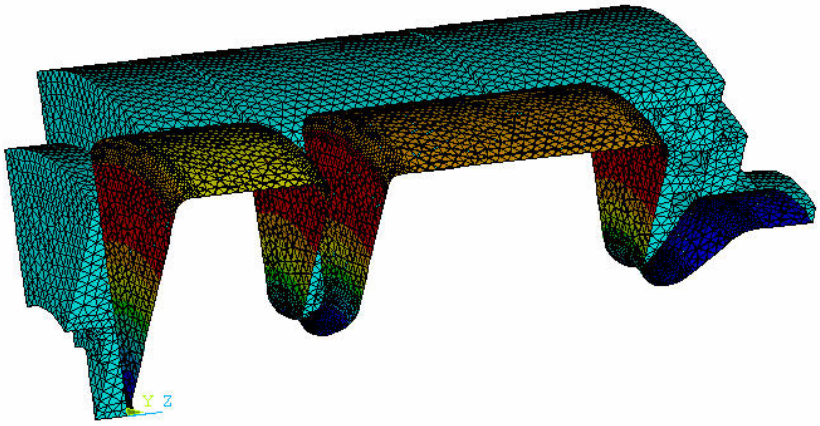

Figure 7 : Surface effect elements (SURF 152) carrying the heat flux values (colored mesh) to be transferred to the cavity wall elements (SOLID 152). To overcome prevalent meshing errors - especially in complex structures - the global mesh size might be refined before meshing the wall elements. The electromagnetic elements (see Figure 3) may be deleted in case of limited mesh nodes as this allows using a fresh number of nodes for meshing the gun jacket.

In this way surface effect elements act as an intermediary to transfer the heat fluxes directly to the wall elements producing a realistic RF induced heat source. The heat drain on the other hand is defined by means of water transfer coefficients α ("convection loads") applied to the individual cooling channels to simulate water flow. The water transfer coefficient generally characterizes the efficiency of the heat convection at the interface between the cavity body and the cooling area. In ANSYS α has to be specified together with the bulk water temperature T_b at each cooling area. Reasonable values should be estimated based on available or desired volume water flow rates provided by the real water distribution system. These are usually limited by technical constraints. To determine α the definition

$$\alpha = \lambda \cdot \frac{Nu}{\phi_H} \quad \left(in \frac{W}{m^2 K} \right) \tag{4}$$

has been used, whereas λ is the thermal conductivity of the coolant (in $W \cdot m^{-1} \cdot K^{-1}$), Nu is the dimensionless Nusselt number and ϕ_H the hydraulic pipe diameter (for non-circular pipes = 4*area/perimeter). The Nusselt number principally relates the heat transferred

between two surfaces at different temperatures for a flowing coolant (convection) to the coolant at rest (conduction). Thus it depends largely on the flow situation. Since the heat transfer coefficient in a meander is beneficially enhanced due to water turbulences, flow rates should be high enough to yield a turbulent flow. A criterion for turbulent water flow in a water tube is given by the Reynolds number:

$$\mathrm{Re} = \frac{\upsilon_m \cdot \phi}{\nu} \quad with \quad \nu = \frac{\eta}{\rho}. \tag{5}$$

Here ν denotes the cinematic viscosity (in $m^2 \cdot s^{-1}$) derived by the dynamic viscosity η ($kg \cdot s^{-1} \cdot m^{-1}$) and water density ϱ. The mean (characteristic) water flow velocity υ_m averaged over the pipe cross-section A_{pipe} can be calculated from the given volume flow rate dV/dt:

$$\upsilon_m = \frac{dV}{dt}\frac{1}{A_{pipe}}. \tag{6}$$

Mainly three regimes characterize the flow situation:

(i) laminar regime: Re ≤ 2320

(ii) transient regime: 2320 < Re < 10000

(iii) turbulent regime: Re ≥ 10000

The Nusselt number defined in eq. (4) actually is a complex measure of the Reynolds number Re, the given geometry and the material-dependent Prandtl number defined by

$$Pr = \frac{\eta \cdot C_p}{\lambda} \tag{7}$$

with C_p denoting the specific heat capacity of the fluid (in $J \cdot kg^{-1} \cdot K^{-1}$). The Prandtl number principally describes the relation of the heat in a viscous fluid generated by friction related to the conducted heat, i.e. a lower Prandtl number characterizes a higher convection efficiency (see Appendix Table 6.1). The Nusselt number Nu(Re,Pr) can only be determined accurately by experiments. Different approximations can be found in literature. For laminar flow

$$Nu = 4.36 \quad or \quad 3.66 \qquad Pr \geq 0.6 \tag{8}$$

at constant surface heat flux or constant surface temperature respectively.

For tubulent flow the following empirical formulas have been used depending also on the tube friction factor f [6]:

$$Nu = \frac{f}{8} \cdot \frac{(Re - 1000) \cdot Pr}{1 + 12.7\sqrt{\frac{f}{8}} \cdot \left(Pr^{\frac{2}{3}} - 1 \right)} \qquad 0.5 < Pr < 2000 \qquad 3000 < Re < 5 \cdot 10^6 \tag{9}$$

$$Nu = \frac{f}{8} \frac{Re \cdot Pr}{1.07 + 12.7\sqrt{\frac{f}{8}} \cdot \left(Pr^{\frac{2}{3}} - 1 \right)} \qquad 0.5 < Pr < 2000 \qquad 10^4 < Re < 5 \cdot 10^6 \tag{10}$$

Eq. (9) yields a better agreement with experimental data at smaller Reynold numbers. The friction factor f of the tube generally depends on the surface condition. It is minimal for smooth surfaces and increases with surface roughness. For smooth pipes f can be expressed - depending on the flow situation - according to [6]:

$$f = \frac{64}{Re} \quad laminar\ flow \tag{11}$$

$$f = \frac{1}{(0.79 \cdot Ln(Re) - 1.64)^2} \qquad 3000 \le Re \le 5 \cdot 10^6 \tag{12}$$

Eventually the transfer coefficients α (eq. (4)) have been evaluated with the help of eqs. 5-12 for the various cooling pipes allowing for the dependence on a given bulk water temperature T_b. See Appendix 6 for the used resource of water properties. According to eq. (5) water flow velocities υ_m should yield Reynold numbers in the range of Re = 10000 or above, on the other hand they should be low enough to prevent from long-term erosion of cavity internal pipes. A reasonable value is υ_m = 2m/s, so that heat transfer coefficients in the order of 1 W·cm^{-2}·K^{-1} are produced for typical cavity water pipe dimensions. This is exemplarily illustrated in Figure 8.

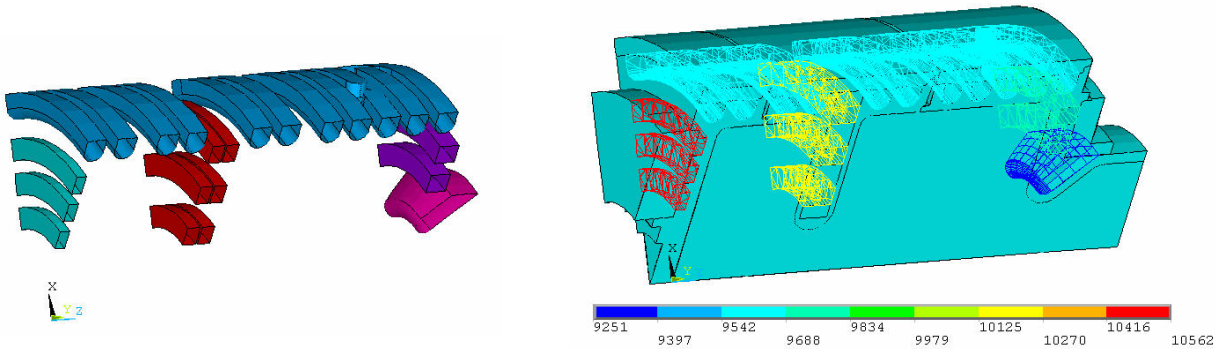

Figure 8 : Cooling meanders within the cavity jacket (left) assigned with appropriate water transfer coefficients to simulate water flow (right, in W·m^{-2}·K^{-1}). These depend on meander geometry, water flow rate and temperature (here: υ_m = 2m/s, T_b = 42 °C). Typical values are in the range of 1 W·cm^{-2}·K^{-1}.

Having defined the transfer coefficients and the thermal conductivity of the cavity material (e.g. $\lambda = 390\ \mathrm{W \cdot m^{-1} \cdot K^{-1}}$ for OFHC copper) the steady-state temperature distribution can be readily calculated. Figure 9 depicts the temperature distribution in *Gun 4* at a mean power of 100 kW assuming $\upsilon_m = 2\mathrm{m/s}$ and $T_b = 42°\mathrm{C}$ throughout. The maximum temperature of 94.3°C is located at the middle iris.

The bulk water temperature has to be regarded as a mean water temperature. Actually the outlet temperature T_{out} may be considerably higher than the inlet water temperature T_{in} which alters the temperature distribution. To resemble this situation in a better way the bulk temperature of adjacent cooling holes belonging to the same meander might be set to different values according to the supposed temperature rise.

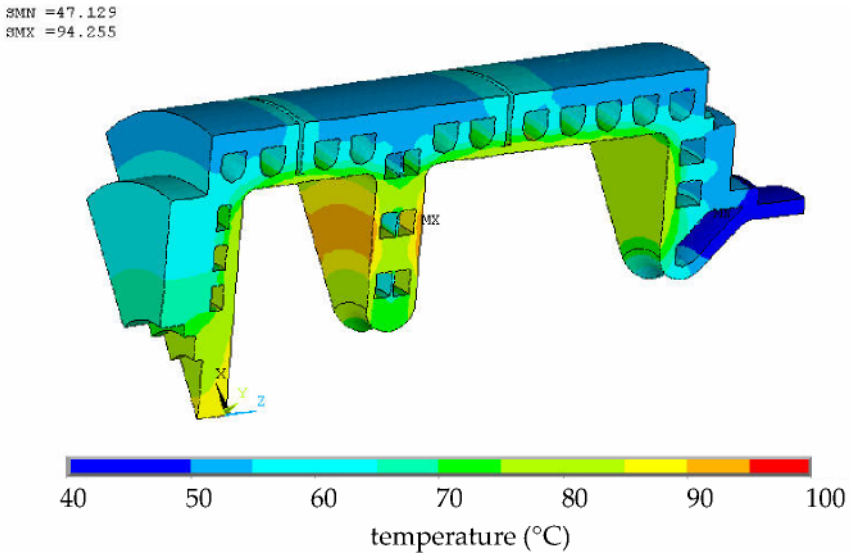

Figure 9 : Temperature distribution in *Gun 4* at a mean power level of 100 kW (42°C bulk water temperature, 390 $\mathrm{W \cdot m^{-1} \cdot K^{-1}}$ thermal conductivity of wall). The heat transfer coefficients have been evaluated by means of eq. (4) assuming water flow velocities of 2 m/s throughout.

If the heat is removed by convection (neglecting air convection and heat radiation effects) the heat rate dQ/dt extracted by the water equals the dissipated mean power P_S. Then the maximum possible temperature rise $\Delta T = T_{out} - T_{in}$ can be assessed by the following calorimetric formula giving the water volume flow rate dV/dt:

$$\Delta T = \frac{P_S \left(= \frac{dQ}{dt}\right)}{\rho C_P \frac{dV}{dt}} \quad \rightarrow \quad \Delta T[°C] \approx 14.5 \cdot \frac{P[kW]}{\frac{dV}{dt}\left[\frac{l}{\min}\right]}. \tag{13}$$

Herein ϱ denotes the water density. E.g. for a total volume flow of $dV/dt = 300$ l/min (max. volume flow at PITZ) the maximum possible temperature rise of the gathered outlet

water is ΔT = 4.8 °C at P_S = 100kW. Still the temperature rise within individual pipes may differ depending on the locally provided volume flow rates and power entries. The latter varies considerably along the cavity boundary as shown in Figure 10 for specific wall segments. An adequate number of water inlets is mandatory to prevent from a disproportionately high increment of ΔT within single water tubes.

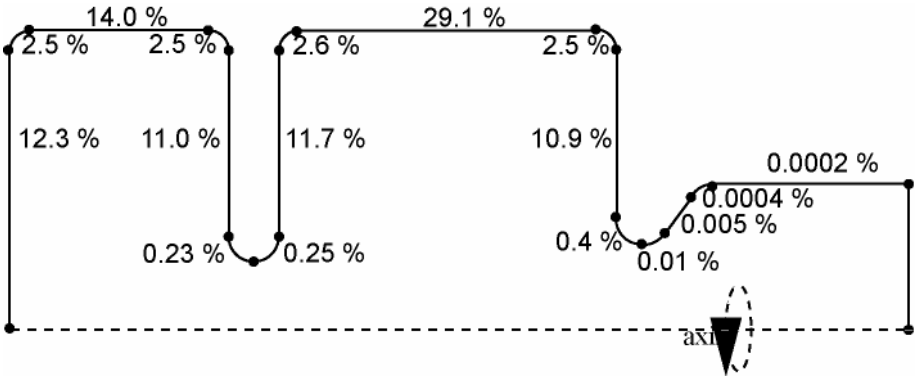

Figure 10: Relative power entries at specified wall segments around the rf-gun internal boundary as calculated with SUPERFISH.

In case the water temperature rise and non-linearities of material properties are not taken into account, the temperature (difference) at any (between) mesh node(s) scales linearly with the applied power. Consequently only a single thermal calculation is necessary to forecast the temperature at any mesh node of the cavity at any power level. This yields a linear dependency in the form

$$T_{xy}(P_S, T_b) = \frac{dT_{xy}}{dP_S} \cdot P_S + T_b \tag{14}$$

The same is true for mean cavity temperatures that might be used to estimate the thermal frequency shift (see section 2.6.1). Due to the simplifications the inaccuracy rises with the power level. Pressure drops Δp within individual tubes should be kept in mind as well as they might impact the achievable volume flow rates. The pressure drop can be estimated by:

$$\Delta p = \frac{f \cdot \rho \cdot L}{2\phi_H} \upsilon_m^2. \tag{15}$$

It rises linearly with the meander length L but quadratically with the flow velocity υ_m.

2.5. Structural Analyses

Structural analyses yield valuable information about the thermal deformation of the cavity body causing frequency shifts and intrinsic stresses. Material properties, boundary constraints and forces acting on the problem geometry as caused by temperature loads have to be set prior to the calculation.

First the mesh elements types have to be "switched" from thermal mass into structural mass elements (in our case 3D 10node tetrahedral SOLID 92). The preceding thermal solution (see section 2.4) can be imported as a load for the structural analysis (*.rth). The resulting cavity distortion depends on the real fixation of the cavity as placed on a support frame. Hence the cavity does not entirely expand freely and realistic structural constraints have to be applied. The fixation scheme can be emulated in ANSYS by assigning displacement degrees of freedom (DOFs) at specified cavity regions to constrain the expansion in a chosen direction of the coordinate system. In either case symmetry planes have to be fixed in all DOFs. Figure 11 illustrates the chosen constraints. The atmospheric pressure (~101325 Pa) has been allowed for acting on the outer cavity shell.

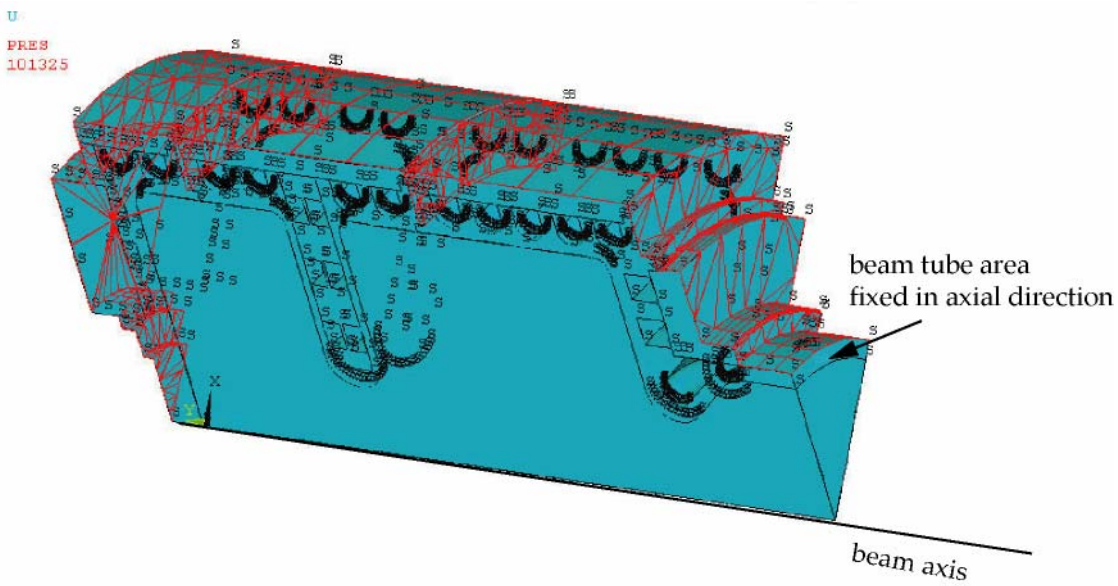

Figure 11: Applied boundary constraints of the problem geometry to initiate the structural analysis. Symmetry planes do not allow any expansion (constraints in all degrees of freedom marked by "S"). In reality the cavity is positioned on a rack. To resemble this situation a single beam tube may be constrained in axial direction only, whereas all other directions are free to expand. By experience this yields quite reliable results. The red net on the outer shell illustrates the barometric pressure set to 1 bar.

The structural material properties to be defined are the thermal expansion factor α_{th} at a ambient/reference temperature T_{ref} (e.g. room temperature), the Young's modulus E (ratio of stress to strain) and the Poisson ratio σ (relative length change along two perpendicular

directions due to strain in one direction). Relevant structural values for OFHC copper are listed in the Table 2 (but also depend on the material history and treatment).

Table 2 : Material parameters of OFHC copper.

Thermal expansion coefficient	α_{th}	K^{-1}	1.67e-5
Young's Modulus	E	GPa	126
Poisson ratio	σ		0.31
Thermal conductivity	λ	$W \cdot m^{-1}K^{-1}$	390
Electrical conductivity	σ_{el}	$\Omega^{-1}m^{-1}$	$5.8e^{7}$
0.2% Proof stress	$R_{P0.2}$	MPa	124

The thermal cavity distortion gives rise to internal wall stresses. These stresses generally are composed by complicated loads such as bending, shearing and twisting forces. ANSYS can evaluate the so-called von Mises stress distribution in the body combining the different loads to an equivalent uniaxial stress as would have been caused by only stretching the material. As this uniaxial stress is directly accessible by measurements of specimens, the results can be compared with the material yield strength (or proof strength) typically stated in literature. The yield strength characterizes the onset of a significant plastic deformation eventually causing a permanent set and should not be exceeded. However, it is not a well-defined point of a material stress-strain curve. Frequently the 0.2% offset yield strength $R_{P0.2}$ (0.2% proof stress) is consulted as an upper tolerable margin resulting in a plastic strain of 0.2%. Figure 12 depicts the von Mises stress due to the thermal load at $P_S = 100kW$ (Figure 9) based on the chosen constraints (Figure 11).

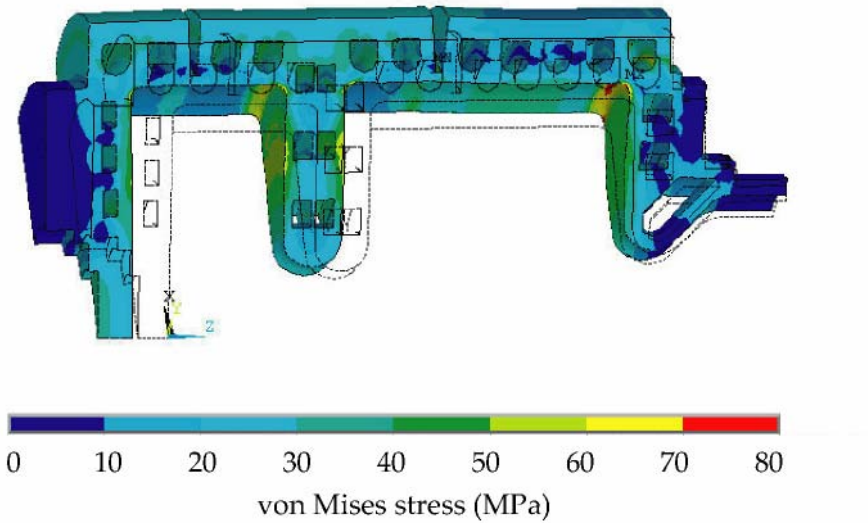

Figure 12: Contour plot of the von Mises stress in *Gun 4* due to a thermal load of 100 kW (T_{ref} = 20°C, load according to Figure 9 and constraints set as in Figure 11). The maximum stress (78 MPa) is located at the roundings of cell two. The undeformed cavity outline is indicated (dashed line). The deformed cavity is drawn to a wider scale (user-defined factor, here: 100) for better visualization.

2.6. Frequency Shifts

Frequency drifts encountered under operation have to be compensated to run the cavity at a stable target frequency f_0 preventing from RF amplitude and phase jitters as far as possible. Photoinjector gun cavities aiming for low transverse emittances do not foresee a mechanical plunger. Due to inevitable fabrication tolerances a coarse tuning might be necessary after the cavity has been built. As for the various RF-guns already built at DESY this is done in air and at room temperature by plastically pressing or stretching the endplates and iris. It demands for relatively large pressure forces to be applied by a dedicated tuning apparatus. Moreover, usually an iterative tuning process is required as the desired field amplitudes in the individual cells have to be equalized within acceptable tolerances ("field balance") [7]. To obtain the desired target frequency f_0 under operation conditions, the expected frequency shift due to the thermal load Δf_{th} and evacuation of the cavity Δf_{evac} have to be taken into account. The non-evacuated cavity at room temperature should be finally tuned to:

$$f_{air} = f_0 + |\Delta f_{th}| - |\Delta f_{evac}|. \tag{16}$$

Estimations for Δf_{th} and Δf_{evac} are given in this section.

2.6.1. RF Induced Thermal Shifts

Due to wall expansion a thermal load reduces the frequency by Δf_{th}, which has to be considered in a final geometrical cavity outline with regard to the supplied nominal water temperature. For this two alternative methods have been accomplished combining ANSYS and SUPERFISH.

The first method utilizes the thermally displaced ANSYS mesh nodes to create the cavity outline directly in SUPERFISH (Figure 13). The undeformed cavity at zero power is used as a reference to calculate Δf_{th}. The outline is traced by typically several hundred ANSYS nodes ample for a reasonable discretization.

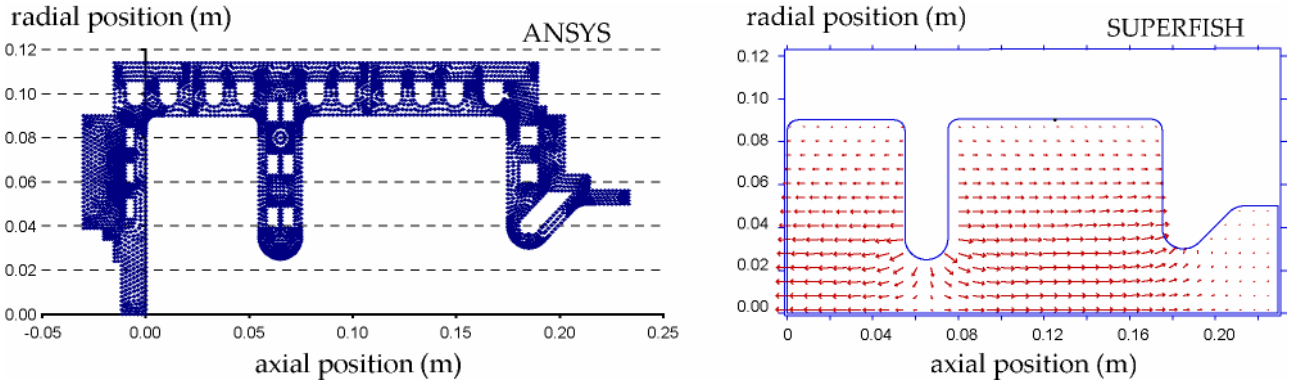

Figure 13: ANSYS cavity nodes at a specified cross-section (left). The internal boundary nodes are utilized for a subsequent SUPERFISH calculation (right).

The second method relates the ANSYS node-to-node displacements due to the thermal deformation along the internal cavity outline with corresponding geometrical frequency sensitivities at a given number of wall segments as defined in SUPERFISH (Figure 14). For this a program has been accomplished. The benefit is that subsequent time-consuming SUPERFISH calculations are obsolete.

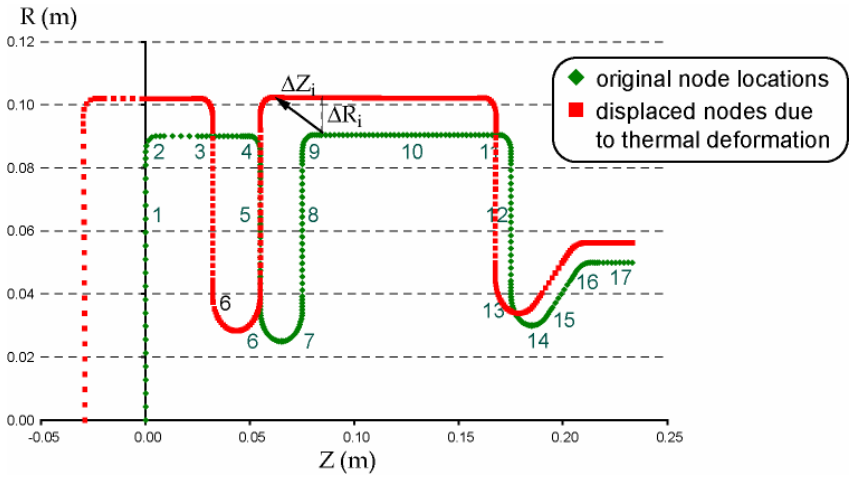

Figure 14: ANSYS nodes of the undeformed and thermally deformed cavity. Displacements are calculated node for node in radial and axial direction and averaged over a finite number of wall segments (numbers) as specified in SUPERFISH. The displacements are drawn relatively to the axially fixed end of the beam tube and scaled for better visualization.

The frequency sensitivities at the wall segments are deduced from Slater's perturbation theorem, whereby a frequency shift δf is caused by a small cavity volume change δV - reducing the volume – according to [3]:

$$\frac{\delta f}{f} = \frac{\int_{\delta V} \left\{ \left[H_\phi(z,r)\right]^2 - \left[E_z(z,r)\right]^2 - \left[E_r(z,r)\right]^2 \right\} dV}{2\int_V \left[H_\phi(z,r)\right]^2 dV}. \qquad (17)$$

Herein H and E denote the magnetic and electric fields in cylindrical coordinates (ϕ,r,z) respectively. The integral in the denominator is over the cavity volume V. In SUPERFISH the frequency shift is listed per wall deformation –enlarging the volume- in radial and axial direction ($\delta f/\delta Z_n$, $\delta f/\delta R_n$) for each cavity boundary segment n. The total frequency shift Δf_t then can be computed by

$$\Delta f_{th} = \sum_{n\ wall\ segments} \frac{\delta f}{\delta R_n} \cdot \overline{\Delta R_{i,n}} + \frac{\delta f}{\delta Z_n} \cdot \overline{\Delta Z_{i,n}}, \qquad (18)$$

in which the ANSYS nodal displacement results ΔZ_i and ΔR_i are to be averaged over each corresponding wall segment n. This works well in radial direction exhibiting a rotational symmetry around the beam axis. However for a multi-cell cavity the node-to-node correlation in axial direction does not work properly as both the resonating cells and irises

expand and nodal displacements ΔZ_i increase in relation to the fixed boundary area (if the cavity is not clamped from both sides) (see Figure 14). Fortunately for TM_{010}-modes the predominant part of the frequency shift is caused by the radial rather than the axial displacements. For the gun cavities used a negligible contribution of ~2% in eq. (18) arises from $\Delta Z_{i,n}$ in case of homogeneous displacements all-around the cavity.

Both methods described above yielded comparable results for the thermal frequency shift Δf_{th} with relative deviations < 7% up to a mean power of P_S = 100kW. Discrepancies are due to simplifications and averaging inherent to eq. (18). Absolute values of Δf_{th} are plotted in Figure 15 at various power levels in relation to the undeformed cavity (T_{ref} = 20°C). A variation of water transfer coefficients with bulk temperature $\alpha(T_b)$ has been considered sampling T_b in steps of 5°C within 27-57°C. Figure 15 reveals the good agreement of both methods (method 1 corresponds to eq. (18)). The Eigenfrequency is decreased when increasing the power and thus the body temperatures. The same effect arises when the inlet water temperature T_b increases. Since the frequency has to be kept fix in practice, T_b has to be set according to the dissipated power P_S.

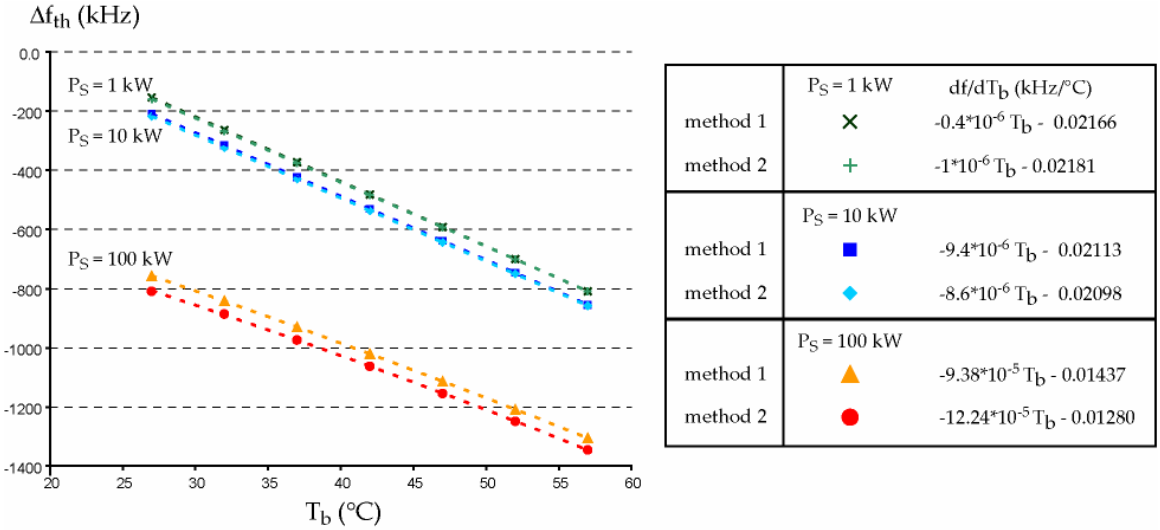

Figure 15: Thermal frequency shifts Δf_{th} at P_S = 1 kW, 10 kW and 100 kW respectively in dependence on T_b sampled in steps of 5°C within 27-57°C (T_{ref} = 20°C). Combining ANSYS and SUPERSISH two alternative methods have been applied as described in the main text. Dashed lines are 2nd–order polynomial fit functions. These can be used to well parameterize $\Delta f_{th}(P_S, T_b)$ or deduce the relation df/dT as listed in the legend.

At a given power level the calculated data can usually be well fitted by 2nd-order polynomial functions. These have been utilized in section 3 to deduce an analytical expression for $\Delta f_{th}(P_S, T_b)$ depending on both the mean power level and water temperature in the range of interest. Similar expressions can also be deduced for cavity temperatures $T_{xy}(P_S, T_b)$. The temperature derivatives of the fit functions have been used here to also deduce the temperature induced frequency shifts $df/dT(T_b)$ given in the legend actually depending also on the power level (comp. section 2.6.4).

2.6.2. Shifts Due to Air Pressure

The combined ANSYS/SUPERFISH calculation method can be used to solely evaluate the impact of the air pressure by simply omitting the thermal load. The air pressure slightly counteracts the thermal expansion, however its effect on frequency is mostly negligible; e.g. ~ +5 kHz at 1 bar for *Gun 4*.

2.6.3. Shifts Induced by Evacuation

As stated above the air pressure does not yield a significant contribution to the total frequency shift. A considerable part however arises from cavity evacuation with the change of permittivity ε. Under vacuum the resonant frequency is increased by

$$\Delta f_{evac} = f_{air} \cdot \left(1 - \frac{1}{\sqrt{\varepsilon_{air}}} \right) \tag{19}$$

compared to the frequency f_{air} in air at same temperature. The permittivity of air ε_{air} depends on the ambient conditions such as air temperature, atmospheric pressure and relative humidity. The frequency converter of SUPERFISH has been used to evaluate Δf_{evac} in dependence on ambient conditions presuming the cavity is isothermal, made of the same bulk material and does not distort when under vacuum. Thus under typical conditions a frequency increase of about $\Delta f_{evac} = 400$ kHz has to be taken into account for a 1.3 GHz cavity as listed in Table 3.

Table 3 : Frequency shift of a cavity at 1.3 GHz due to evacuation in dependence on relative humidity.

Relative humidity* %	Permittivity of air ε_{air}	Frequency shift Δf_{evac} kHz
10	1.0005569	362
20	1.0005773	375
30	1.0005976	388
40	1.0006179	402
50	1.0006382	415
60	1.0006586	428
70	1.0006789	441
80	1.0006992	454
90	1.0007196	468
100	1.0007399	481

* 20°C cavity and air temperature, 101325 Pascal barometric pressure

2.6.4. Water Temperature-Induced Shifts

Once the cavity is tuned and in operation, remaining frequency drifts can only be compensated by water temperature as no mechanical plunger is provided. For an RF gun with pillbox-like cells, the temperature induced frequency shift df/dT can be estimated analytically. In a cavity with radius R the TM_{010}-mode is given by

$$\frac{df_{TM010}}{dT} = -\frac{c \cdot x_{01}}{2\pi}\frac{d(R^{-1})}{dT} = -\frac{f_{TM010}}{R}\frac{dR}{dT} \tag{20}$$

with the speed of light c and the first null x_{01} of the zeroth order Besselt function of first kind. Inserting $R \approx R_0 + R_0 \alpha_{th} \cdot (T-T_0)$ with room temperature values marked by "$_0$" gives

$$\frac{df_{TM010}}{dT} \approx -f_{TM010} \cdot \alpha_{th}, \tag{21}$$

as a rule of thumb. E.g. df/dT = -21.7 kHz/°C at 1.3 GHz for copper (Table 2) in good accordance with measured values for *Gun 2*, i.e. df/dT = 22-23 kHz/°C [8]. Consequently only a rather small frequency range can be spanned by water control that has to comprise the target frequency.

Equation (21) holds for a uniform expansion of the cavity. However inhomogeneous cavity distortions are prevalent especially at higher power levels. This can result in partially smaller local expansions and thus lower values of df/dT as would be the case for a solely uniform expansion at a constant body temperature. The situation is illustrated in Figure 16 comparing the nodal distortions of *Gun4* at a relatively low and high power level respectively. As described in section 2.6.1 the temperature-induced frequency shifts $df/dT(P_s,T_b)$ can be derived numerically (see Figure 15). For *Gun 4* this resulted in $df/dT(T_b)$ = 21.7-21.8 kHz/°C at P_s = 1kW and $df/dT(T_b)$ = 16-20 kHz/°C at 100 kW.

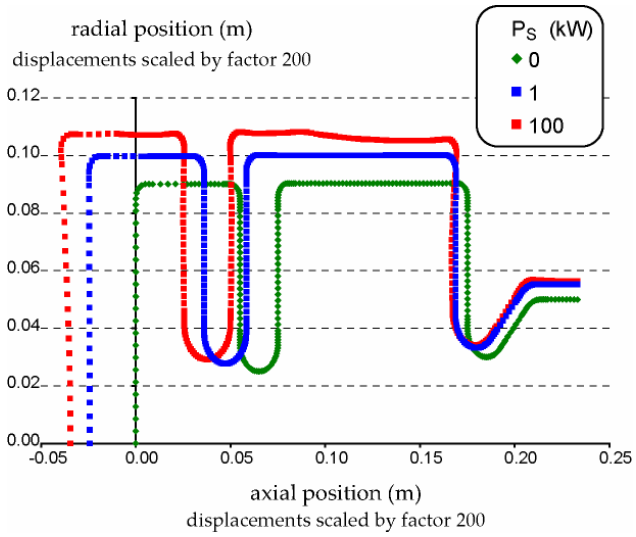

Figure 16: Displacement results at P_S= 1 kW and P_S= 100 kW (T_{ref} = 20°C, T_b = 52°C).

3. Results

3.1. DESY GUN 2

Gun 2 (Figure 17) has been fully characterized at PITZ operating with 900 μs long pulses at 10 Hz repetition rate (0.9 % duty cycle) and a field amplitude of 40 MV/m at the photocathode corresponding to 27 kW mean power. This pulse operation fulfilled the TTF2 VUV FEL requirements, whereas no fundamental limit on the field gradient was detected [9]. The gun has been transferred to DESY Hamburg in November 2003, installed in January 2004 and the first beam was accelerated in March 2005 [10].

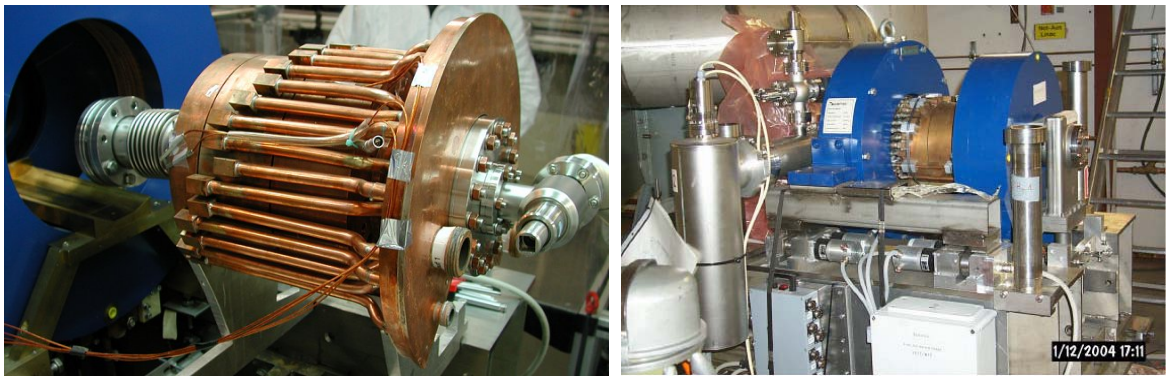

Figure 17: *Gun 2* at PITZ Zeuthen showing the water distribution manifold and outer cooling pipes (left) and in the TTF tunnel (right) after transfer to DESY Hamburg.

Figure 18 shows the quarter ANSYS model of *Gun 2* including the tuning holes in the side plates. In the following ANSYS results are presented assuming uniform flow velocities of 2 m/s throughout (design value). It does not fully resemble the experimental situation at PITZ which could not been reproduced numerically. This is due to the unknown water flow rates in the individual tubes as no flow meters had been installed. Actually an unexpected low volume flow rate has been provided as measured at a later phase [11].

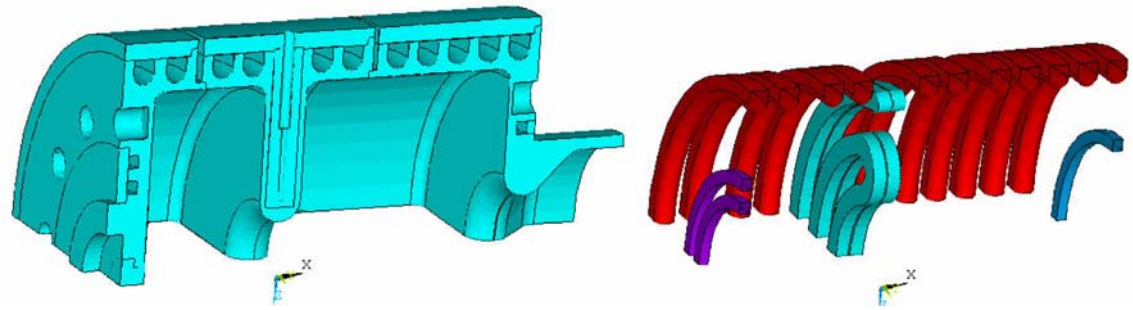

Figure 18: ANSYS ¼-model of *Gun 2* (left) including 14 cooling tubes (right), i.e. 11 tubes around the cavity circumference, 1 meander at the cathode plane (2 turns), 1 tube at the end plate of cell 2 and 1 meander in the iris (3 turns).

The principal temperature distribution and von Mises stresses in the cavity body -here at a mean power of P_S=100 kW and bulk water temperature of T_b = 42°C- are shown in Figure 19. Hot spots are visible at the tuning holes and the beam tube iris, where cooling is rather inefficient. Due to the comparably large temperature gradients also significant stresses would arise in the cavity body.

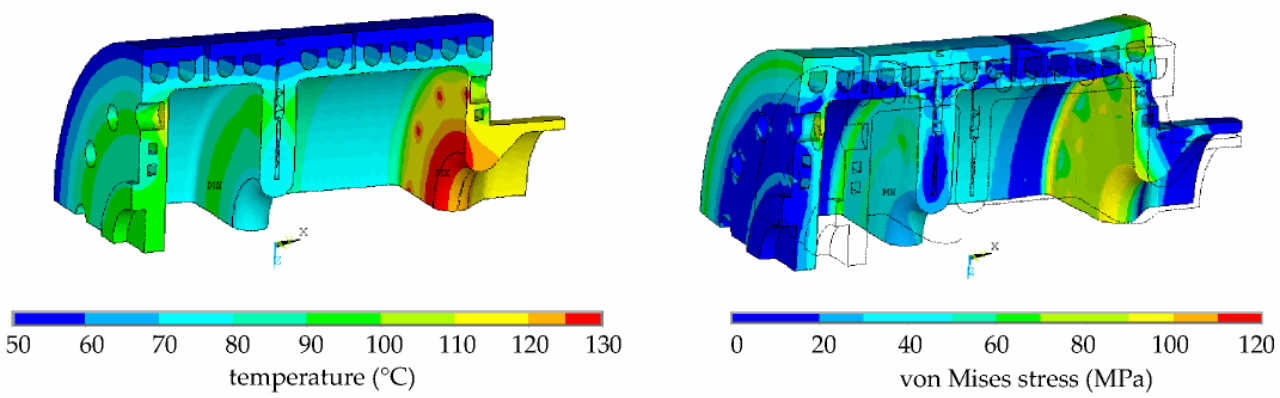

Figure 19: Temperature distribution (left) and von Mises stresses (right) in *Gun 2* at a mean power level of 100 kW (T_b = 42°C, υ_m = 2m/s). The undeformed cavity outline is indicated on the right (dashed line). The deformed cavity is drawn to a wider scale for better visualization.

Figure 20 shows the more relaxed situation at the nominal operation power of 27 kW.

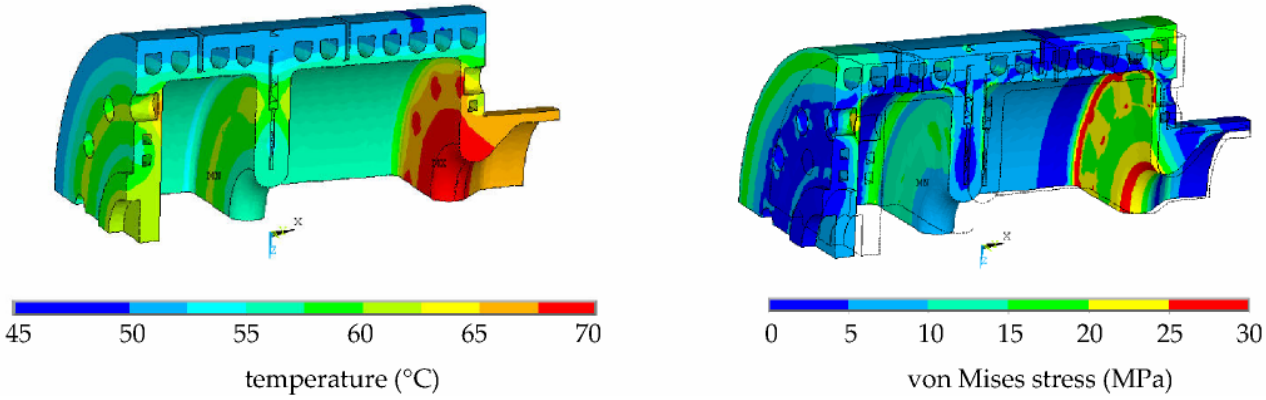

Figure 20: Results similar to Figure 19 at P_S = 27 kW (T_b = 47°C).

A water temperature rise ΔT in individual tubes has been neglected, so that $T_{in} = T_{out} = T_b$. Actually a finite ΔT alters the real temperature distribution accordingly. In Table 4 an estimate of the maximum possible ΔT within each meander is given based on local power entries (see Figure 10) at 27 kW and 100 kW mean power respectively presuming uniform flow velocities of 2m/s. Using eq. (6) this results in local volume flow rates dV/dt finally yielding the expected water temperature rise by means of eq. (13). Especially at higher power levels the contribution would be significant.

Table 4 : Estimate of the maximum possible water temperature rise in each meander of *Gun 2* at a power level of 27 kW and 100 kW respectively (υ_m = 2m/s in each meander).

meander type	inlets	dV/dt (l/min)	ΔT (°C) @ P_S = 27 kW	ΔT (°C) @ P_S = 100 kW
Iris	1	15.6	5.8	21.5
Half cell	4	52.4	1.4	5.3
Full cell	7	91.8	1.5	5.4
Cathode plate	1	3.6	13.4	49.5
End plate	1	3.6	12.3	45.6
All	14	167	2.3	8.7

The main concept to stabilize the target frequency under operation is to re-adjust the incoming water temperature T_{in} whenever the accelerating field is perturbed by thermal drifts or in case the mean power level is changed. The mean power level is defined by the chosen RF pulse pattern and peak power defining the field amplitude at the photocathode. At zero power T_{in} is comparably hot and is successively reduced when increasing the power. Once a set value is reached T_{in} is kept stable. At PITZ residual temperature drifts within 0.05°C (peak to peak) have been measured [12] according to a maximum frequency jitter of ~1 kHz.

The amount of the needed change of the inlet water temperature to stabilize the frequency at different power levels has been derived numerically. For this a parameterization of the thermal frequency shift $\Delta f_{th}(P_S,T_b)$ has been done as explained in section 2.6.1 in relation to the undeformed cavity at zero power and room temperature (T_{ref} = 20°C). An overview of the situation is shown in Figure 21 by means of frequency shift contours separated by Δf_{th} = 100 kHz.

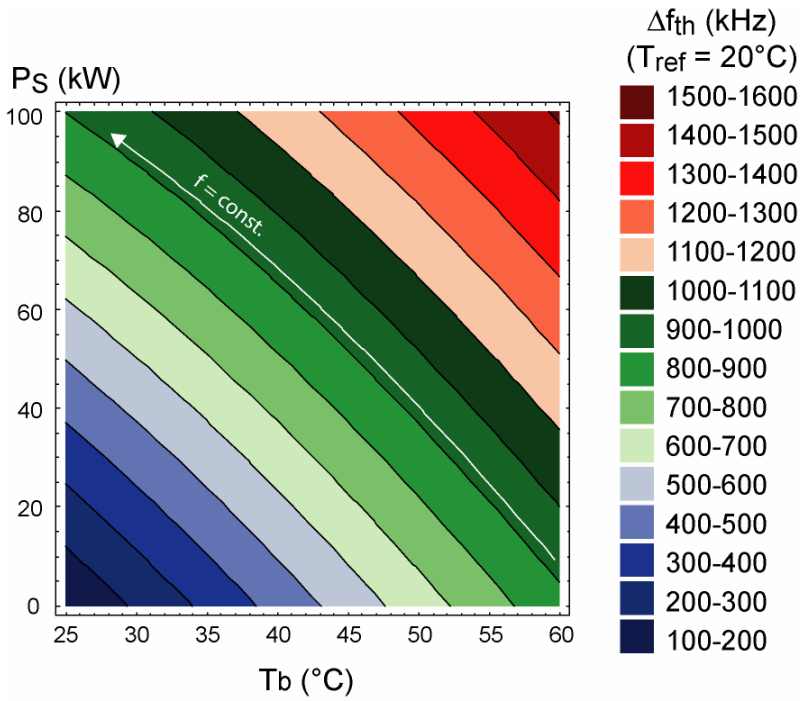

Figure 21: Thermal frequency shift Δf_{th} (T_{ref} = 20°C) in dependence on the mean power level P_S and bulk water temperature T_b (u_m = 2 m/s throughout).

The inlet water temperature T_{in} has to be kept constant once the desired mean power level is reached. A later operation at a higher power level can only be achieved by further cooling down T_{in}. Water temperatures however are usually limited by technical constraints, e.g. $T_{min} = 27°C$ and $T_{max} = 64°C$ at PITZ [11]. To achieve $P_S = 100$ kW at $T_{in} = 27°C$, T_{in} equals 63°C at zero power only closely within these limit. As *Gun 2* was not prepared to run at such a high power the target frequency at zero power was already obtained at $T_{in} = 55.5°C$ to finally achieve $P_S = 27$ kW at $T_{in} \approx 47°C$ (see Figure 20). This is in principal agreement with the simulation results.

3.2. DESY GUN 4

Gun 3 as the direct descendent of *Gun 2* does not differ significantly in terms of the water cooling layout. Thus the thermal and structural characteristics are similar to those presented in section Figure 17 and shall be omitted here. *Gun 3* is currently ready for tuning and will be tested at PITZ thereafter.

Gun 4 however is destined for an operation at increased power levels allowing higher repetition rates and/or accelerating fields. The cooling concept has been revised to mainly supply more water to both end plates of the cavity. A new water manifold has been conceived using 11 water supply pipes to better control the flow rates in the individual meanders. Figure 22 depicts the water distribution manifold and cavity with partly omitted covers revealing the inner meanders. The cavity exhibits no tuning holes or rings at the end plates to locally reinforce the wall thereby improving the heat conduction. This concept however bears a risk with regard to a necessary plastic wall deformation for cavity tuning, which requires significantly high pressure forces.

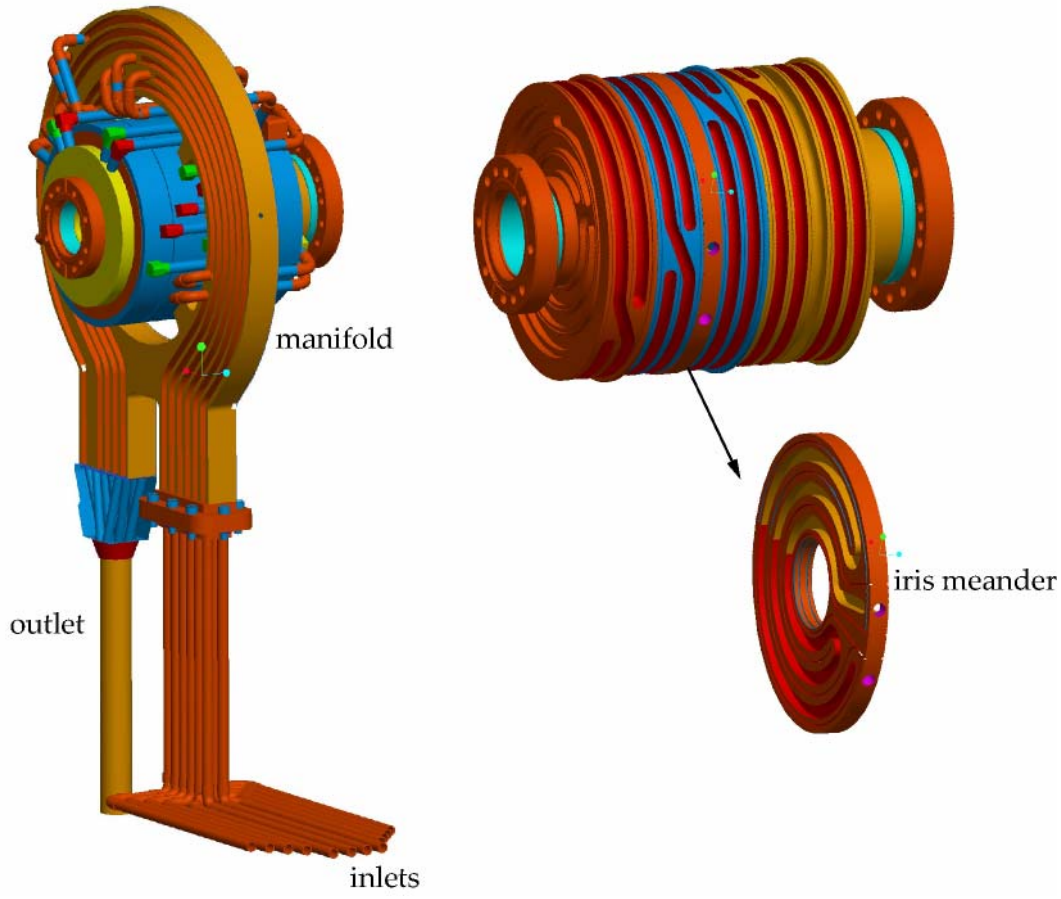

Figure 22: *Gun 4* with water distribution manifold. Partly the covers have been omitted to reveal the inner meanders. The iris meander is shown apart down left. The cavity is equipped with 6 meanders around the cavity circumference, 2 in the cathode plate, 2 in the end plate and 1 in the iris.

In the following results are given for the present geometry, still the cavity might be subject to further design changes. Similar to *Gun 2* uniform flow velocities of 2 m/s were used throughout. The principal temperature distribution and von Mises stresses in the cavity body have already been presented in section 2 (Figure 9 and Figure 12) for P_S=100 kW and T_b = 42°C. The body temperatures are much more relaxed than those of *Gun 2* shown in Figure 19. A comparison of the nodal displacements in *Gun 4* and *Gun 2* is illustrated in Figure 23 using the same premises. Due to the enhanced cooling of the endplates and the absence of tuning holes non-homogeneous wall distortions are significantly reduced.

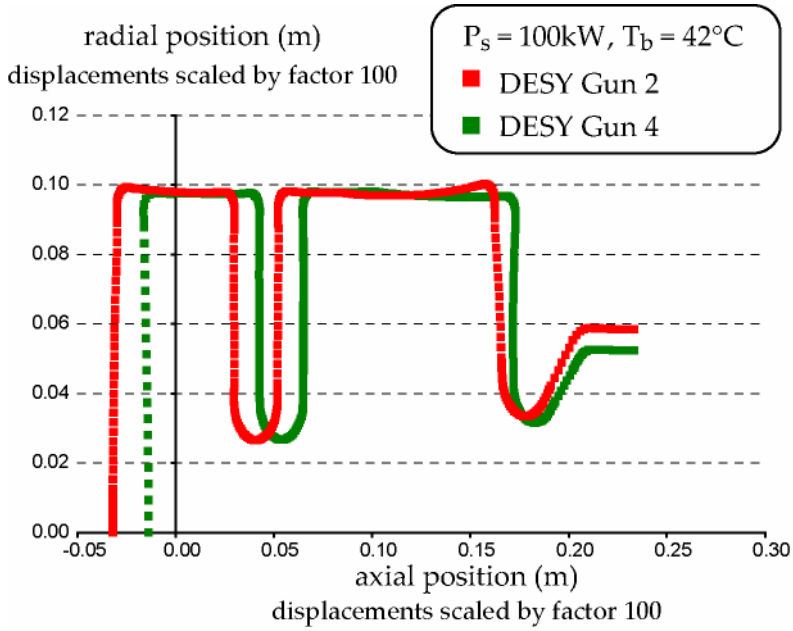

Figure 23: Thermal displacements of *Gun 4* and *Gun 2* at P_S = 100 kW and T_b = 42°C yielding Δf_{th} = 1021 kHz and Δf_{th} = 1183 kHz respectively (T_{ref} =20°C). Displacements are shown relative to the axially fixed end of the beam tube.

Table 5 lists the expected -so far not considered- water temperature rise ΔT within each meander of *Gun 4* at 100 kW mean power presuming uniform flow velocities of 2m/s to be compared with Table 4. The main benefit is obvious at both endplates. The iris is currently subject of revision aiming for more water inlets to specifically decrease ΔT [13].

Table 5 : Estimate of the maximum possible temperature rise in each meander of *Gun 4* at a power level of 100 kW (υ_m = 2m/s in each meander).

meander type	inlets	dV/dt (l/min)	ΔT (°C) @ P_S = 100 kW
Iris	1	15.6	21.5
Half cell	2	26.2	10.5
Full cell	4	52.4	9.5
Cathode plate	1	12.0	14.9
End plate	1	12.0	6.6
End plate Iris	1	31.8	2.7
All	11	150.1	9.7

Figure 24 finally shows the thermal frequency shifts $\Delta f_{th}(P_S, T_b)$ similar to Figure 21 for *Gun 2*, which have been reduced considerably. Furthermore, the more homogeneous cavity deformation actually results in larger temperature shift df/dT at high power levels. This means, that a higher power level would be reachable with a minor temperature decrement once the cavity is tuned.

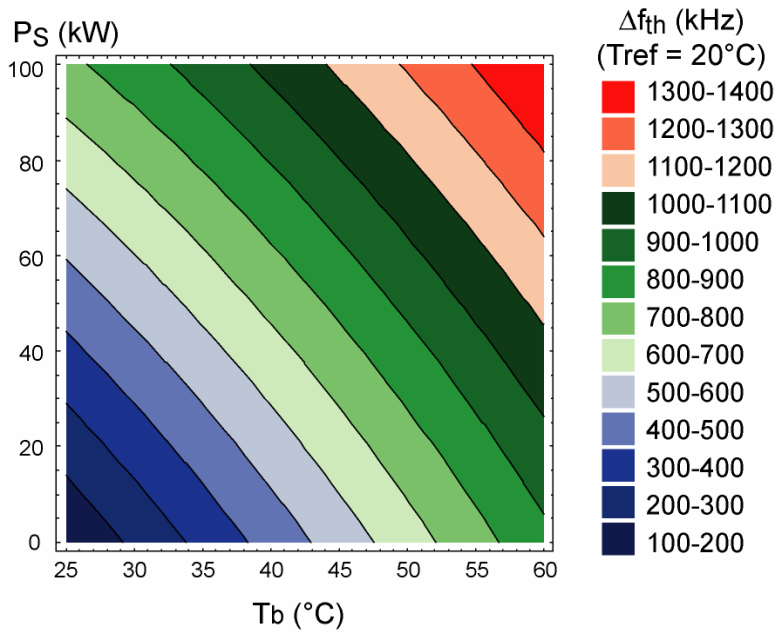

Figure 24: Thermal frequency shift Δf_{th} (T_{ref} = 20°C) in dependence on the mean power level P_S and bulk water temperature T_b (u_m = 2 m/s throughout).

4. Conclusion

Calculation techniques for comprehensive electromagnetical, thermal and structural Finite Element Analyses of RF cavities have been described extensively. This includes the estimation of frequency shifts caused by different sources such as RF-power, temperature, air pressure and change in permittivity due to evacuation. Two alternative methods have been presented to assess the RF induced thermal frequency shift using ANSYS in combination with SUPERFISH. For an RF gun in absence of a mechanical tuner this not only helps to tune the cavity properly at room temperature but also forecasts the maximum mean power achievable when decreasing the inlet water temperature to its lower limit. An analytical way has been followed to evaluate water transfer coefficients in dependence on temperature necessary as an input for the numerical calculations. This facilitates to deduce analytical expressions for cavity frequency shifts and temperatures in a realistic way depending both on the power and water temperature.

FEA results have been summarized for two different RF guns; already in operation at the Tesla Test Facility VUV-FEL (*Gun 2*) and in the final design stage at DESY (*Gun 4*). The temperature distribution, internal body stresses and expected thermal frequency shifts have been presented at various power levels and water temperatures. The water temperature rise within individual tubes depends on the locally delivered volume flow rates and has been estimated analytically for different scenarios. This would alter the presented numerical results accordingly.

Gun 4 aims to operate at a mean power level in the range of 100 kW exhibiting an improved cooling scheme compared to *Gun 2*. The thermally stabilized operation at such high power levels has still to be demonstrated experimentally. *Gun 4* shall be fully characterized at the Photoinjector Test Stand Zeuthen (PITZ).

5. Acknowledgement

The author would like to thank Michael von Hartrott for many helpful discussions and Marc Dirsat for the transfer of the CAD models into ANSYS. Many thanks also to the colleagues at DESY Zeuthen and Hamburg especially Frank Stephan and Alexander Donat for making available all model data for the calculations.

6. Appendix

Table 6.1 summarizes the resource of water properties used to determine the heat transfer coefficients α by means of eq. (4) in dependence on water temperature.

Table 6.1 : Resource of used water properties.

Bulk water temperature T_b K	Density ρ kg/litre	Specific heat capacity C_p J/(kg·K)	Dynamic viscosity η kg/(m·s)	Thermal conductivity λ W/(m·K)	Prandtl number Pr
275	0.9998	4211	0.001652	0.574	12.97
280	0.9999	4198	0.001422	0.582	12.12
285	0.9999	4189	0.001225	0.59	10.26
290	0.9995	4184	0.00108	0.598	8.70
295	0.9988	4181	0.000959	0.606	7.56
300	0.9980	4179	0.000855	0.613	6.62
305	0.9970	4178	0.000769	0.62	5.83
310	0.9950	4178	0.000695	0.628	5.18
315	0.9930	4179	0.000631	0.634	4.62
320	0.9911	4180	0.000577	0.64	4.16
325	0.9891	4182	0.000528	0.645	3.77
330	0.9872	4184	0.000489	0.65	3.42
335	0.9843	4186	0.000453	0.656	3.15
340	0.9823	4188	0.00042	0.66	2.89
345	0.9794	4191	0.000389	0.668	2.67
350	0.9766	4195	0.000365	0.668	2.44
355	0.9737	4199	0.000343	0.671	2.29
360	0.9709	4203	0.000324	0.674	2.15
365	0.9671	4209	0.000306	0.677	2.02
370	0.9634	4214	0.000289	0.679	1.90
373	0.9606	4217	0.000279	0.68	1.79

7. References

[1] http://www.ansys.com/

[2] N. Hartman, R. Rimmer, "Electromagnetic, Thermal, and Structural Analysis of Rf-Cavities using ANSYS, Proceedings of the 19th Particle Accelerator Conference, Chicago, Illinois, USA, 18-22. June 2001 http://accelconf.web.cern.ch/AccelConf/p01/PAPERS/MPPH060.PDF

[3] K. Halbach, R.F. Holsinger, Particle Accelerators 7 (1976), page 213, distributed by the Los Alamos Accelerator Code Group (LAACG) (http://laacg1.lanl.gov/laacg/services.html)

[4] http://www.ptc.com/

[5] Microwave Studio and MAFIA, Gesellschaft für Computer-Simulationstechnik (CST), Darmstadt, Germany, http://www.cst.com/

[6] F.P. Incropera, D.P. Witt, "Fundamentals of Heat and Mass Transfer, 5th Edition, 2002, John Wiley & Sons, New York, ISBN 0-471-38650-2

[7] I. Bohnet, "Tuning of a 1.5 Cell Copper Cavity", DESY Zeuthen, PITZ Note, March 2002

[8] F. Stephan, private communication

[9] M. Krasilnikov at al., "Characterization of the Electron Source at the Photoinjector Test Facility at DESY Zeuthen", FEL 2003, Tsukuba, Sept. 2003

[10] S. Schreiber, talk on "RF Gun Commissioning", PITZ collaboration meeting, 30. March 2004

[11] J. Helm, RCI GmbH, private communication

[12] J.P. Carneiro et al."Behaviour of the TTF2 RF Gun with Long Pulses and High Repetition Rates", TESLA Report, TESLA 2003-33, DESY, December 2003 http://accelconf.web.cern.ch/AccelConf/p03/PAPERS/WPAB034.PDF

[13] J. Meißner, private communication